Modeling of the Lower Ionosphere during Solar X-ray Flares of Different Classes

Susanna Bekker[1] and Iliya A. Ryakhovskiy[1]

[1]Sadovsky Institute of Geospheres Dynamics of Russian Academy of Sciences

November 22, 2022

Abstract

This paper presents the results of modeling the lower ionosphere response to solar X-ray flares of C-, M- and X-classes. The model is based on a 5-component scheme of the ionization-recombination cycle of the ionospheric D-region. Input parameters of the plasma-chemical model under different heliogeophysical conditions corresponding to selected X-ray flares were determined by using data received from AURA, SDO and GOES satellites. Verification of the obtained results was carried out with use of ground-based radiophysical measurements taken at the geophysical observatory Mikhnevo. Results of comparing the calculated and experimental the radio wave amplitude variations along six European very low frequency (VLF) paths show that the root mean square error (RMSE) does not exceed 1.5 dB for ~70% of cases including X-class flares during which the amplitude jump on some paths reaches 8 dB. Qualitative and quantitative analysis of the verification results of the VLF signal amplitude has showed the good predictive capability of the built model for describing weak and moderate ionospheric disturbances.

1 **Modeling of the Lower Ionosphere during Solar *X*-ray Flares of Different Classes**

2 **S. Z. Bekker[1,2] and I. A. Ryakhovsky[1]**

3 [1] Sadovsky Institute of Geospheres Dynamics, Russian Academy of Sciences, Moscow, Russia.

4 [2] Moscow Institute of Physics and Technology, Moscow, Russia.

5 Corresponding author: Susanna Bekker (susanna.bekker@gmail.com)

6 **Key Points:**

7 - A plasma-chemical model of the ionospheric *D*-region is presented

8 - Model allows to predict ionosphere parameters behavior during *C*- and *M*-class flares
9   with sufficient accuracy

10 - Verification of the obtained results was carried out with use of ground-based
11   radiophysical measurements

12 **Abstract**

13 This paper presents the results of modeling the lower ionosphere response to solar *X*-ray flares of
14 *C*-, *M*- and *X*-classes. The model is based on a 5-component scheme of the ionization-
15 recombination cycle of the ionospheric *D*-region. Input parameters of the plasma-chemical
16 model under different heliogeophysical conditions corresponding to selected *X*-ray flares were
17 determined by using data received from AURA, SDO and GOES satellites. Verification of the
18 obtained results was carried out with use of ground-based radiophysical measurements taken at
19 the geophysical observatory Mikhnevo. Results of comparing the calculated and experimental
20 the radio wave amplitude variations along six European very low frequency (VLF) paths show
21 that the root mean square error (RMSE) does not exceed 1.5 dB for ~70% of cases including *X*-
22 class flares during which the amplitude jump on some paths reaches 8 dB. Qualitative and
23 quantitative analysis of the verification results of the VLF signal amplitude has showed the good
24 predictive capability of the built model for describing weak and moderate ionospheric
25 disturbances.

26 **1 Introduction**

27   At present, researchers intensively develop modeling of all layers of ionosphere for
28 solving research problems of various profiles, as well as for applied tasks, in particular,
29 improvement of the estimates' accuracy of propagation of radio waves in a wide range of
30 frequencies.

31   Despite the fact that now there is a significant number of theoretical estimates and
32 experimental data on the processes occurring in ionospheric plasma and about the spatial and
33 temporal distribution of concentrations of its components (Bilitza et al., 2017; Marsh et al., 2013;
34 Nava et al., 2008; Wait & Spies, 1964), the prediction accuracy of ionospheric parameters,
35 especially under conditions of various disturbances, is low.

36   The lower part of the ionosphere ($h \sim 60$–90 km) remains the least studied by now.
37 Difficulties in studying the *D*-region is due to a large number of photochemical processes and
38 incapability of continuous measuring the ionosphere parameters, first of all, concentration of
39 electrons *Ne*, at these amplitudes (Egorova et al., 2011; Friedrich et al., 2018; Krivolutsky et al.,
40 2015; Turunen et al., 1992, 1996; Verronen et al., 2005, 2016).

41   State of the lower ionosphere parameters is determined by the latitude and space weather
42 factors, such as solar cosmic rays, magnetospheric storms, precipitation of charged particles,
43 ionizing electromagnetic radiation (Kumar et al., 2015, 2017; Kumar & Kumar, 2018; Maurya et
44 al., 2012, 2018; Peter et al., 2006; Thomson et al., 2004, 2005). Solar flares are accompanied by
45 considerably increased intensity of *X*-radiation, which leads to a significant change of the
46 electron concentration in the illuminated area of the lower ionosphere (Grubor et al., 2005, 2008;
47 Mitra, 1974; Nina et al., 2011; Poppoff & Whitten, 1962; Ryakhovskiy et al., 2018). Such *Ne*
48 variations significantly distort the amplitude and phase characteristics of the very low frequency
49 (VLF) signals within a range 3–30 kHz propagating in the Earth-ionosphere waveguide with the
50 *D*-region as its upper boundary (Brunelli & Namgaladze, 1988; Gavrilov et al., 2019a; Han et al.,
51 2011; Hargreaves, 1995; Schunk & Nagy, 2009; Wait & Spies, 1964). This allows using the
52 measurements of amplitude and phase of VLF signals for studying the state of lower ionosphere,
53 and applying them as a tool for verification of the medium models (Bekker et al., 2018; Lyakhov
54 et al., 2018; Palit et al., 2013). Verification on the basis of data of ground-based radiophysical

55 measurements allows the direct assessment of the model's predictive capability at solving
56 problems of the VLF signal propagation. Moreover, the quantity of radiophysical data is many
57 orders of magnitude greater than the electron concentration measurements taken for the *D*-
58 region, which makes it possible to carry out verification under almost any heliogeophysical
59 conditions including the solar flares.

60   This work is devoted to modeling the lower ionosphere during solar *X*-ray flares of
61 different classes and analysis of the results obtained by verification with the ground-based
62 radiophysical measurements taken at the Mikhnevo geophysical observatory of Sadovsky
63 Institute of Geospheres Dynamics (Gavrilov et al., 2017, 2019a).

2 Experimental data obtained at the Mikhnevo Geophysical Observatory

65   Since 2014, Mikhnevo has been continuously monitoring the amplitude and phase
66 characteristics of electromagnetic signals from the VLF transmitters located throughout the
67 world (Gavrilov et al., 2019b).

68   To verify the results of the modeling we used measurements of the amplitude of the
69 signals received at the Moscow region observatory Mikhnevo (55°N 38°E) from six transmitters
70 located at the European midlatitudes (Figure 1). The main characteristics of the transmitters are
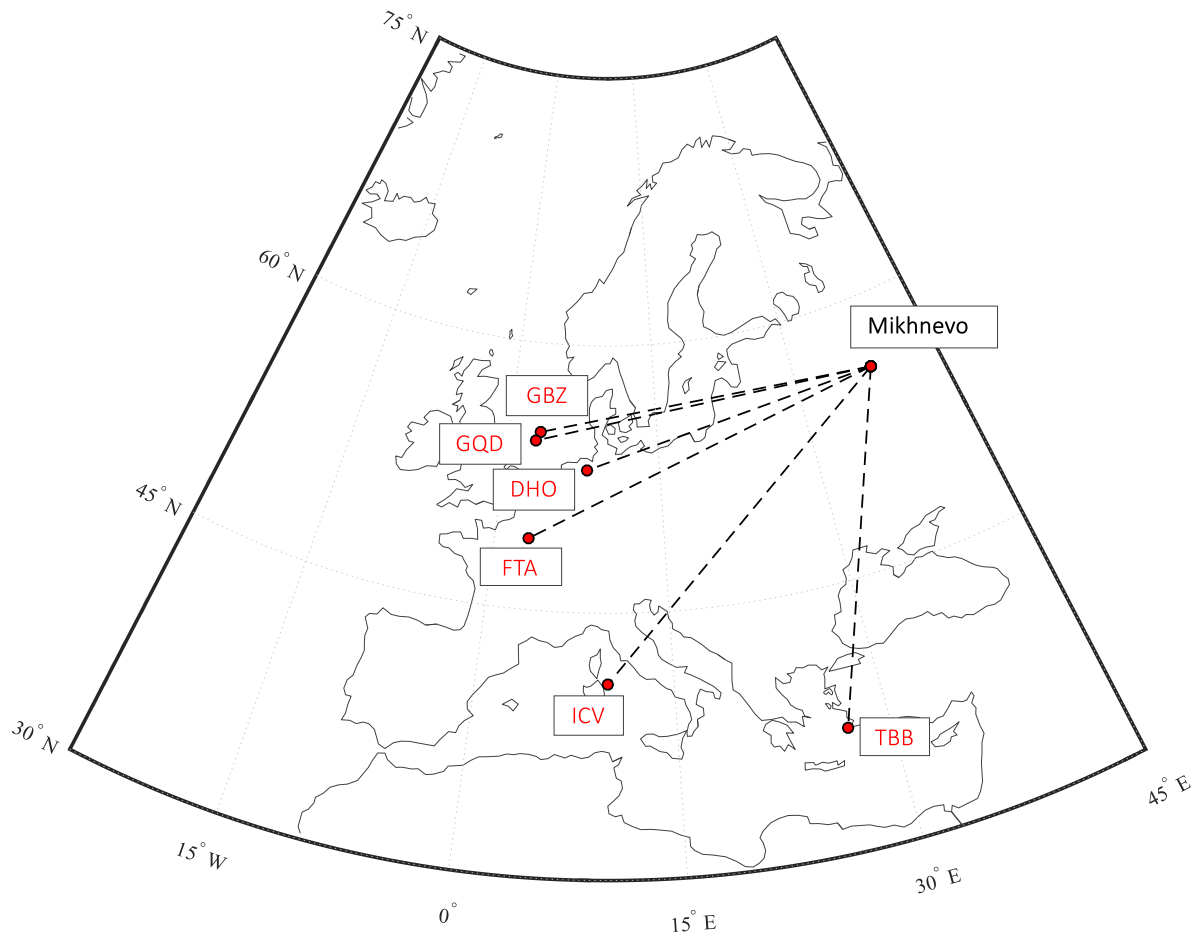71 listed in Table 1.

Figure 1. The locations of the Mikhnevo geophysical observatory and the VLF transmitters.

74 **Table 1**

75 *Main Characteristics of the VLF Signal Transmitters*

Station	Location	Coordinates	Frequency [kHz]	Path length [km]
GBZ	England	55°N 3°W	19.6	2585
ICV	Italy	41°N 10°E	20.3	2580
FTA	France	49°N 3°E	20.9	2500
GQD	England	55°N 3°W	22.1	2565
DHO	Germany	53°N 8°E	23.4	1960
TBB	Turkey	37°N 27°E	26.7	2100

76   The amplitude of the signal passing through the simulated medium was calculated by
77 using the LWPC program (Ferguson, 1998). The configured nominal power of the transmitters
78 was 1 kW. Amplitude values were taken in [dB] for the purpose of quantitative comparison of
79 theoretical and experimental daily variations. The amplitude shift due to the difference between
80 the unknown actual transmitter power and the one used for the calculations was determined by
81 the difference of the theoretical amplitude value and the experimental data obtained at a quite
82 heliogeophysical day that preceded each considered flare (Palit et al., 2013).

83 **3 Plasma-chemical model of the lower ionosphere**

84   As stated in the introduction, at present there are a significant number of empirical and
85 theoretical models of the lower ionosphere, describing its state with some accuracy. For solving
86 applied problems of the radio wave propagation, the two-parameter Wait-Ferguson model
87 (Ferguson, 1995; Wait & Spies, 1964) is most often used. On the one hand, this model makes it
88 possible to simulate the radioequivalent ionosphere to successfully use its results for calculating
89 the radio wave propagation. On the other hand, the modeled vertical electron concentration
90 profiles can be not corresponding to the real ones, since the model is based on the exponential *Ne*
91 profile.

92   When choosing the number of plasma-chemical processes on which the model under
93 development is based, it is necessary to take into account not only the expected accuracy of the
94 results, but also the possibility of rapid calculation of the environmental parameter variations at
95 natural disturbances. Today, there are global three-dimensional numerical models of the lower
96 ionosphere, taking into account hundreds and thousands of known photochemical reactions.
97 These models describe the behavior of ionospheric components under the calm conditions and
98 under the influence of various disturbances (Krivolutsky et al., 2015; Turunen et al., 1992, 1996;
99 Verronen et al., 2016). However, such models require extremely high computational power and
100 time resources, and therefore, the applied tasks of forecasting radio wave propagation cannot be
101 promptly solved with it. Moreover, the number of unknown reaction rate constants increases
102 with the number of considered plasma-chemical processes, which can lead to higher errors.

103   The system of differential equations of the ionization-recombination cycle describes the
104 behavior of charged and neutral components, the dynamics of which are most important at *D*-
105 region heights. Analysis of the results of calculating the electron concentration in the 4-
106 component (Glukhov et al., 1992), 5-component (Egoshin et al., 2012) and 8-component
107 (Kudryavtsev and Romanyukha, 1995) plasma-chemical models of the lower ionosphere has

108   showed no significant difference between the results of the two latter. However, not accounting
109   the variations of concentration of the negative cluster ions, absent in the 4-component model,
110   leads to a noticeable decrease of the *Ne* concentration at altitudes less than 70 km, which
111   fundamentally affects the results of calculation of the VLF radio wave propagation both under
112   the calm conditions and at *X*-ray flares.

113   Therefore, the 5-component ionization-recombination cycle of the ionospheric *D*-region
114   (1) has been selected for this work as the most optimal. The system describes the behavior of
115   concentration of electrons *Ne* and 4 ion types: NO^+, O_2^-, positive and negative cluster ions XY^+,
116   XY^-. It takes into account almost all major photochemical processes occurring in the lower
117   ionosphere.

$$
\begin{cases}
\dfrac{d[NO^+]}{dt} = q - 4\cdot10^{-7}\left(\dfrac{300}{T}\right)^{1/5}[NO^+]N_e - B[NO^+] - 10^{-7}[NO^+]\left([O_2^-]+[XY^-]\right); \\[2mm]
\dfrac{d[XY^+]}{dt} = B[NO^+] - 2.55\cdot10^{-5}[XY^+]N_e - 10^{-7}[XY^+]\left([O_2^-]+[XY^-]\right); \\[2mm]
\dfrac{d[O_2^-]}{dt} = 1.4\cdot10^{-29}\left(\dfrac{300}{T}\right)\exp\left(-\dfrac{600}{T}\right)[O_2]^2 N_e - 0.33[O_2^-] - 4\cdot10^{-10}[O_3][O_2^-] - \\[2mm]
-10^{-7}[O_2^-]\left([NO^+]+[XY^+]\right) - 4\cdot10^{-31}[O_2]^2[O_2^-]; \\[2mm]
\dfrac{d[XY^-]}{dt} = 4\cdot10^{-10}[O_3][O_2^-] + 4\cdot10^{-31}[O_2]^2[O_2^-] - 10^{-7}[XY^-]\left([NO^+]+[XY^+]\right) - [XY^-]; \\[2mm]
\dfrac{dN_e}{dt} = \dfrac{d[NO^+]}{dt} + \dfrac{d[XY^+]}{dt} - \dfrac{d[O_2^-]}{dt} - \dfrac{d[XY^-]}{dt}; \\[2mm]
B = 1.8\cdot10^{-28}\left(308/T\right)^{4.7}[H_2O][N_2] + \dfrac{2\cdot10^{-31}\left(300/T\right)^{4.4}[N_2]^2 \times 10^{-9}[H_2O]}{C} + \\[2mm]
+\dfrac{10^{-9}[H_2O]}{3.1\cdot10^4 T^{-4}\exp\left(-4590/T\right)[N_2]+10^{-9}[H_2O]} \times \\[2mm]
\times\left(7\cdot10^{-30}\left(300/T\right)^3[CO_2][N_2] + \dfrac{2\cdot10^{-31}\left(300/T\right)^{4.4}[N_2]^2 \times 10^{-9}[CO_2]}{C}\right); \\[2mm]
C = 1.5\cdot10^6 T^{-5.4}\exp\left(-2450/T\right)[N_2]+10^{-9}\left([CO_2]+[H_2O]\right).
\end{cases}
\tag{1}
$$

118   3.1 Input data

119   The system input parameters are the ionization rate *q*, concentration of neutrals *M*,
120   temperature *T*, and concentration of small neutral components $[H_2O]$, $[CO_2]$, $[O_3]$.

121   It is known that ionization rate is the key parameter responsible for change of the *Ne*
122   concentration during solar flares, that is why its calculation must be particularly careful. At the
123   same time, for a correct modeling of the lower ionosphere during disturbances of various nature,
124   we need to know the state of the medium before and after the perturbation, in other words we
125   must correctly calculate the background *Ne* values. There are at least two reasons for this. First,
126   the accuracy of calculating the background concentration of *Ne* significantly affects the quality
127   of modeling small solar flares (Palit et al., 2013). Second, vertical profiles of *Ne* during the calm

128   Sun are used to normalize the radio wave amplitude during verification of the results (see
129   paragraph 2). At the same time, the accuracy of calculation of background electron concentration
130   values in addition to the ionization rate significantly depends on the temperature and
131   concentration of neutrals (Bekker, 2018). Therefore, a great attention was paid to the accuracy of
132   determining not only q, but also other parameters of the system (1).

133   In order to obtain the most reliable values of T, $[N_2]$, $[O_2]$, $[H_2O]$ and $[O_3]$, a statistical
134   analysis of the experimental atmospheric data obtained by the AURA satellite from 2004 to 2018
135   (Livesey et al., 2013) was performed.

136   It is obvious that at solving the system of ionization-recombination cycle under some
137   specific heliogeophysical conditions, use of averaged values rather than separate measurements
138   from satellite as input parameters seems to be more correct. Besides, it is necessary to approach
139   such averaging carefully, because the results of calculation of the electron concentration
140   significantly depend on the selected ranges of the heliogeophysical conditions - latitude,
141   longitude, zenith angle, season, index $F10.7$. On the one hand, the selected ranges of
142   heliogeophysical conditions should be wide enough to include a representative sample of
143   measurements, and on the other hand, a considered parameter should not change significantly
144   within the given limits. To solve this problem, the daily, seasonal, latitudinal, and longitudinal
145   dependences of satellite data T, $[N_2]$, $[O_2]$, $[H_2O]$, and $[O_3]$, as well as the dependence on solar
146   activity, were considered. For each of the parameters, the probability density functions were built
147   and their dynamics were analyzed when each heliogeophysical condition changed in its turn with
148   the other conditions fixed.

149   Figure 2 shows the neutrals temperature T dependence on latitude for different months at
150   an altitude of $h = 60$ km. The colors in the figure correspond to the values of the probability
151   density function of temperature $P(T)$ normalized to its maximum. As can be seen, the
152   temperature has the latitudinal dependence, therefore, the latitude step $\Delta\varphi$ must be selected in
153   such a way that the temperature does not change significantly. For example, during the summer
154   months, when choosing $\Delta\varphi = 10°$ the difference between the nearby latitudinal T values does not
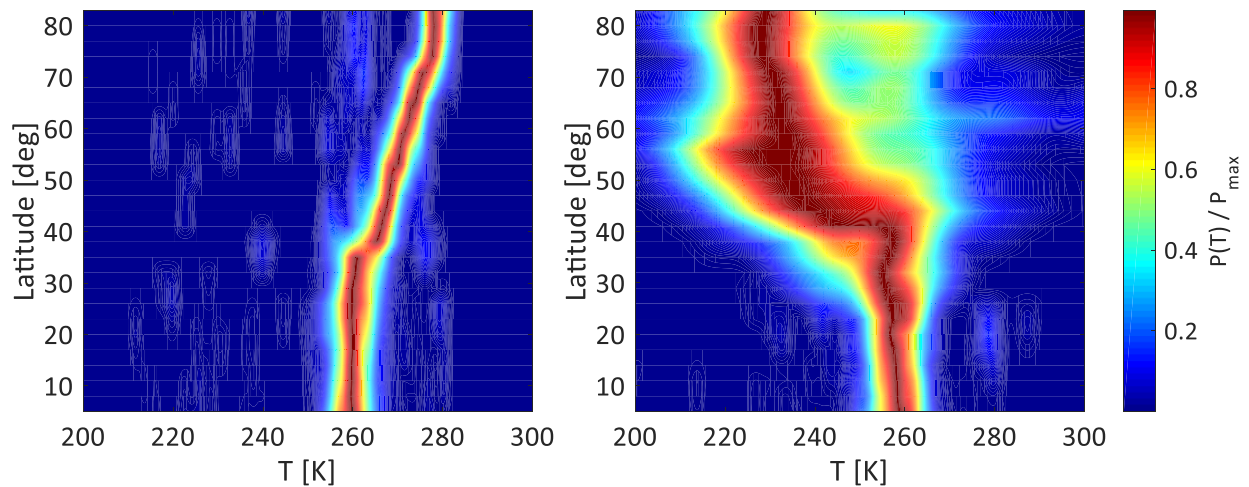155   exceed 3.5%.

156

Figure 2. Dependence of the normalized probability density function $P(T)$ on latitude based on
(left panel) the June data and (right panel) the December data ($h = 60$ km).

159   Besides, one should pay attention to how the function $P(T)$ varies with a season. Not only
160   does the average value profile differ, but also its dispersion; the spread of values for the winter
161   period is much larger than that of summer. This point was also taken into account for the
162   simulation and temperature values were considered for each month separately.

163   The analysis of behavior of $P(T)$ function at various sets of heliogeophysical conditions
164   has showed that temperature has a clear dependence on season and latitude within the considered
165   altitude range and at any level of solar activity.

166   The next parameter essentially influencing Ne at the D-region altitudes is concentration
167   of neutrals M. It is found that the average concentration does not depend on latitude, however the
168   increased spread of values is clearly observed at approach to the poles. The seasonal value
169   change is seen only at $h \leq 80$ km and not for the entire range of latitudes. Figure 3 shows the
170   seasonal variation of neutrals concentration M for different latitude ranges at an altitude of 75
171   km. The colors in the figure correspond to the values of the probability density function $P(M)$
172   normalized to its maximum. As follows from the Figure 3, the seasonal M profile is seen at
173   latitudes $\varphi > 40°$, and within the equatorial part, its value is almost constant. Since the
174   concentration at low latitudes does not depend on the season, it is natural that the dispersion of
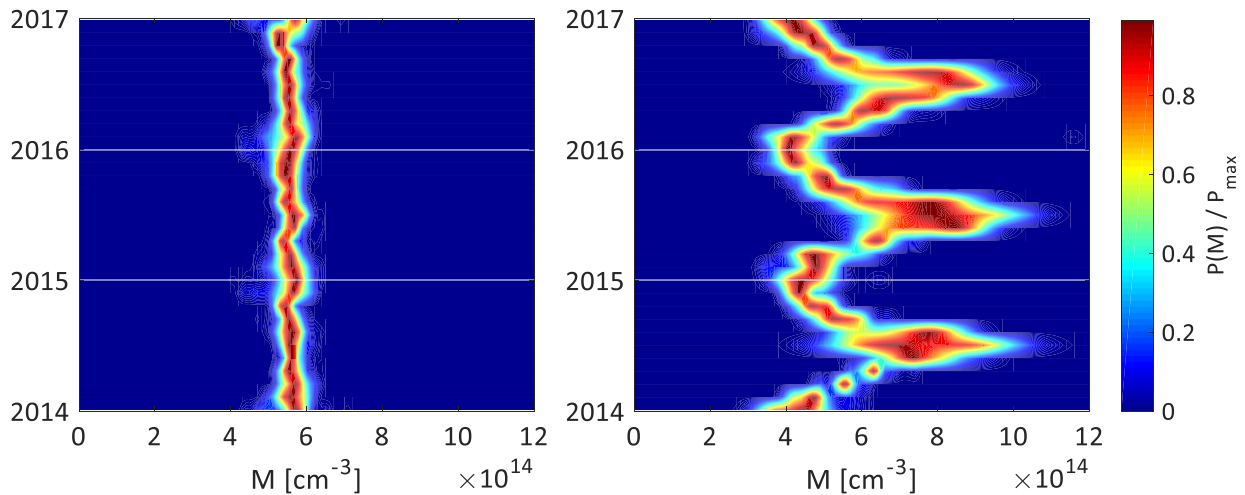175   concentrations here is lesser.

176

Figure 3. The seasonal dependence of the normalized probability density function $P(M)$ for (left
panel) $0° < \varphi < 40°$ and (right panel) $\varphi > 40°$ ($h = 75$ km).

179   The daily variations of temperature and concentration of neutrals is not detected at any of
180   the altitudes. As for solar activity; as a rule, the dispersion of values increases with its growth,
181   but the median remains practically unchanged.

182   The behavior of small neutral components is nearly the same as that of the concentration
183   of neutrals M, since experimental satellite measurements of [H_2O], [O_3] and [CO_2], as well as
184   measurements of [NO] concentration required for calculation of q are given in [ppmv]
185   (Anderson et al., 1986; Bekker, 2018; Brunelli & Namgaladze, 1988). Other regularities
186   registered make insignificant contribution to the already discovered dependences, so their
187   discussion will not be given.

188   The performed statistical analysis of T, [N_2], [O_2], [H_2O] and [O_3] has allowed making
189   careful and individual selection of acceptable ranges of heliogeophysical conditions for each

190 parameter, thus providing for the most correct approach to calculating the profiles of input
191 parameters of the ionization-recombination cycle system within the available data received from
192 satellite.

193 3.2 Calculation of the ionization rate

194 As noted above, one of the key parameters of the system of equations (1) is the ionization
195 rate q. The main sources of charged particles at altitudes $h < 100$ km are the cosmic rays (q_{CR}),
196 flux of solar L_α (q_α) and L_β (q_β), flux of hard ultraviolet (q_{UV}) and X-rays emissions (q_{XR}). At
197 increased solar activity, particles falling out of the radiation belts also significantly influence
198 ionization at the polar latitudes (Bekker, 2018; Paulsen et al., 1972; Thomas & Bowman, 1985).
199 In this work, all of the above sources have been taken into account at calculation of the total
200 ionization rate.

201 It is obvious that the value of q_{XR} actually determines the total ionization rate during the
202 X-ray flare. Satellite data on the radiation flux within three wavelength ranges were used to
203 calculate the q_{XR} during a flare. The measurements in the channels $\lambda_A = 0.05$–0.4 nm and $\lambda_B =$
204 0.1–0.8 nm were taken on the GOES satellites (Machol & Viereck, 2016), while the
205 measurements in the channel $\lambda_C = 0.1$–7 nm – on the SDO satellite (Woods et al., 2012). The
206 work of Korsunskaya (2019) contains the description of the algorithm of calculating q_{XR} by the
207 solar spectrum from the measurements taken on GOES and SDO satellites.

208 The ultraviolet part of the spectrum was also calculated on the basis of data obtained
209 from the GOES satellite.

210 3.3 Calculation of electron concentration

211 Altitude profiles of electron concentration were calculated for separate VLF paths, for
212 which further verification of the results was carried out. We calculated the profiles along the
213 paths with steps of ~ 300 km that could vary slightly so that the profiles were distributed evenly.

214 For the simulation we selected several X-ray flares of different classes (C-, M- and X-
215 class), meeting the following conditions:

216 1. available X-ray solar flux measurements from the GOES and SDO satellites to be used
217 for the ionization rate calculation;

218 2. full illumination of the European VLF paths during the flares;

219 3. operable condition of VLF signal transmitters and a receiver located at the Mikhnevo
220 geophysical observatory, allowing verification of the results.

221 According to these criteria, we selected several X-ray flares of different classes, that
222 occurred in October 2013 and June 2014. Table 2 features the data of the flares under
223 consideration. The data of the quiet days on 22 October 2013 and 8 June 2014 preceding the
224 events listed in Table 2 were used for normalization of the amplitude values.

225 We selected these two series of consecutive flares of different classes because we also
226 wanted to check if the temporal dynamics of small neutral atmospheric components during the X-
227 radiation growth should be included in the ionospheric models. In our model, the concentrations
228 of small neutrals are considered the external input parameters and are not modified during the

229 calculation process. If the hard radiation noticeably modifies the small neutrals during a flare,
230 calculation of the sequence of events should give an increasing error for each subsequent flare.

231 **Table 2**

232 *Data of the Analyzed Solar Flares*

Date	Start time (UT)	Maximum time (UT)	Maximum flux
24 October 2013	09:59	10:09	*M*2.5
24 October 2013	10:30	10:33	*M*3.5
25 October 2013	07:53	08:01	*X*1.7
25 October 2013	09:43	10:12	*M*1.0
9 June 2014	12:24	12:29	*C*9.0
10 June 2014	08:17	08:25	*C*3.9
10 June 2014	09:17	09:31	*C*5.1
10 June 2014	10:04	10:17	*C*5.0
10 June 2014	11:36	11:42	*X*2.2
10 June 2014	12:36	12:52	*X*1.5

233 Basing on the analysis above, we determined acceptable ranges of heliogeophysical
234 conditions for the selected geographical points and moments of time. The values T, $[N_2]$, $[O_2]$,
235 $[H_2O]$, $[O_3]$ and $[CO_2]$, that fell within the above ranges, were used to construct the probability
236 density functions with an altitude step $\Delta h = 5$ km. These functions were used for calculation of
237 the most probable values which we applied to solve the system of differential equations of the
238 ionization-recombination cycle. Ionization rate q was determined as a function of time with step
239 $\Delta t = 1$ min. The system of equations (1) was solved for each set of the obtained vertical profiles
240 of input parameters. At the output, we obtained the electron concentrations under calm
241 conditions and during solar flares of different classes.

242 Figure 4 features the *X*-ray flux registered by GOES satellite, the vertical profile of the
243 ionization rate and electron concentration above the Mikhnevo geophysical observatory during
244 solar flares of *X*- and *M*-classes on 25 October 2013. The electron concentration registered
245 during *X*-ray flares increased by more than 2 orders of magnitude at some altitudes of the *D*-
246 region.

247 Figure 5 features the *Ne* concentration dynamics at an altitude $h = 75$ km during the day
248 of 25 October 2013, calculated by using the temperature *T* and concentration of neutrals *M*,
249 obtained from the AURA satellite and the MSIS model (Hedin, 1991).

250 The curves obtained show a difference between the *T* and *M* values from MSIS model
251 and the most probable values obtained from satellite. Besides, in Figure 5, one can see a
252 significant contribution to the accuracy of *Ne* concentration calculation, made by not only the
253 ionization rate, but also by temperature and concentration of neutral components. Therefore, we
254 assume that the statistical analysis of the input parameters based on the satellite data should
255 fundamentally improve the *D*-region simulation quality at least for the calm conditions and the
256 *C*- and *M*-class flares when the concentration of *Ne* is the most sensitive to the considered
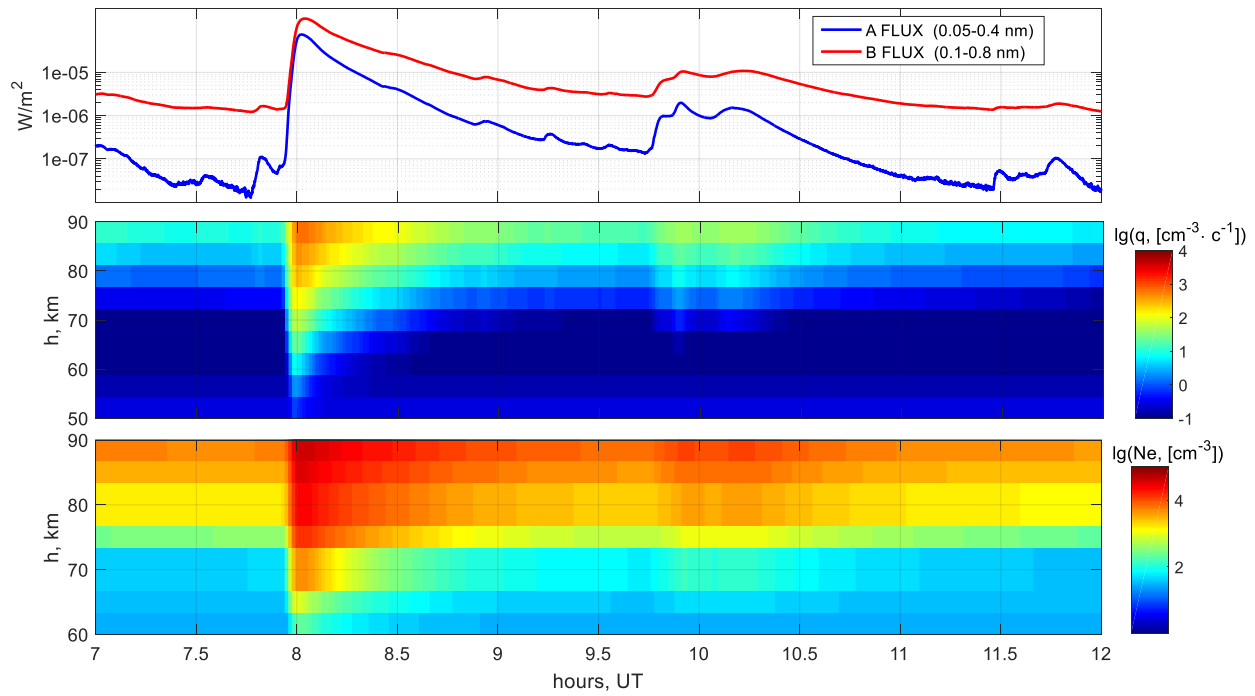257 variations.

258

259 **Figure 4.** (top panel) *X*-ray flux, (middle panel) ionization rate and (bottom panel) electron
260 concentration during *X*- and *M*-class flares on 25 October 2013 above the Mikhnevo geophysical
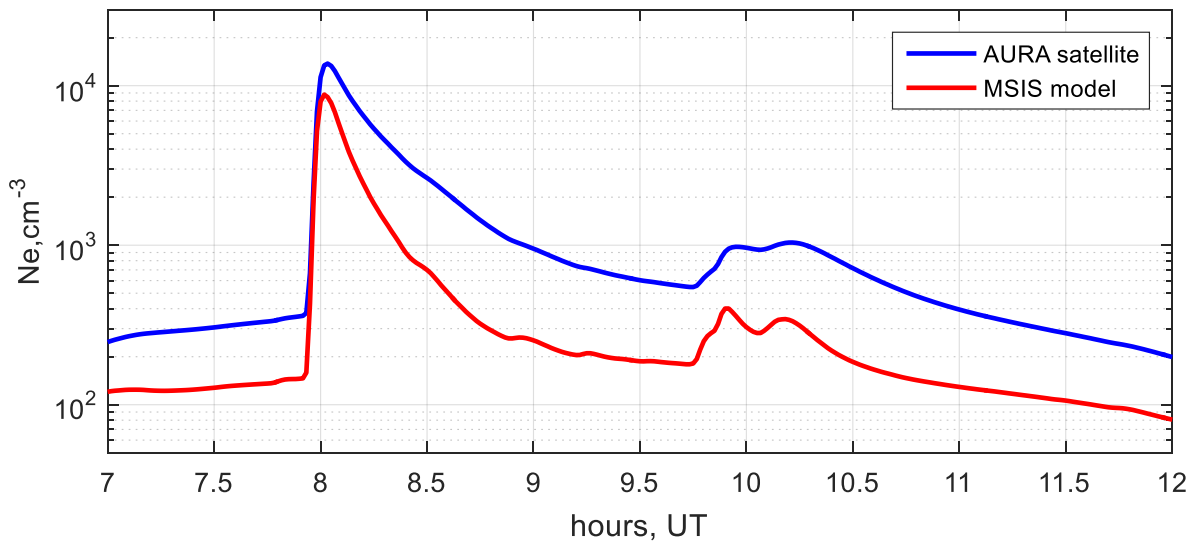261 observatory.

262

263 **Figure 5.** Electron concentration during *X*- and *M*-class flares on 25 October 2013 above the
264 geophysical observatory Mikhnevo, calculated by using the MSIS model and the data received
265 from the AURA satellite.

266   **4 The model verification based on the experimental data on VLF radio wave propagation**
267   **during *X*-ray flares and discussion of the results**

268   As mentioned above, we used the amplitude characteristics of the VLF transmitter signals
269   (Table 1) received at the Mikhnevo geophysical observatory for verification of the results of
270   modeling the lower ionosphere at the flares listed in Table 2.

271   Figure 6 presents the results of comparing the obtained theoretical and experimental
272   curves for three flares of different classes that occurred on 25 October 2013 and 9 June 2014.
273   The diagrams show the time variation of the signal from three VLF transmitters - GQD, ICV,
274   FTA.

275
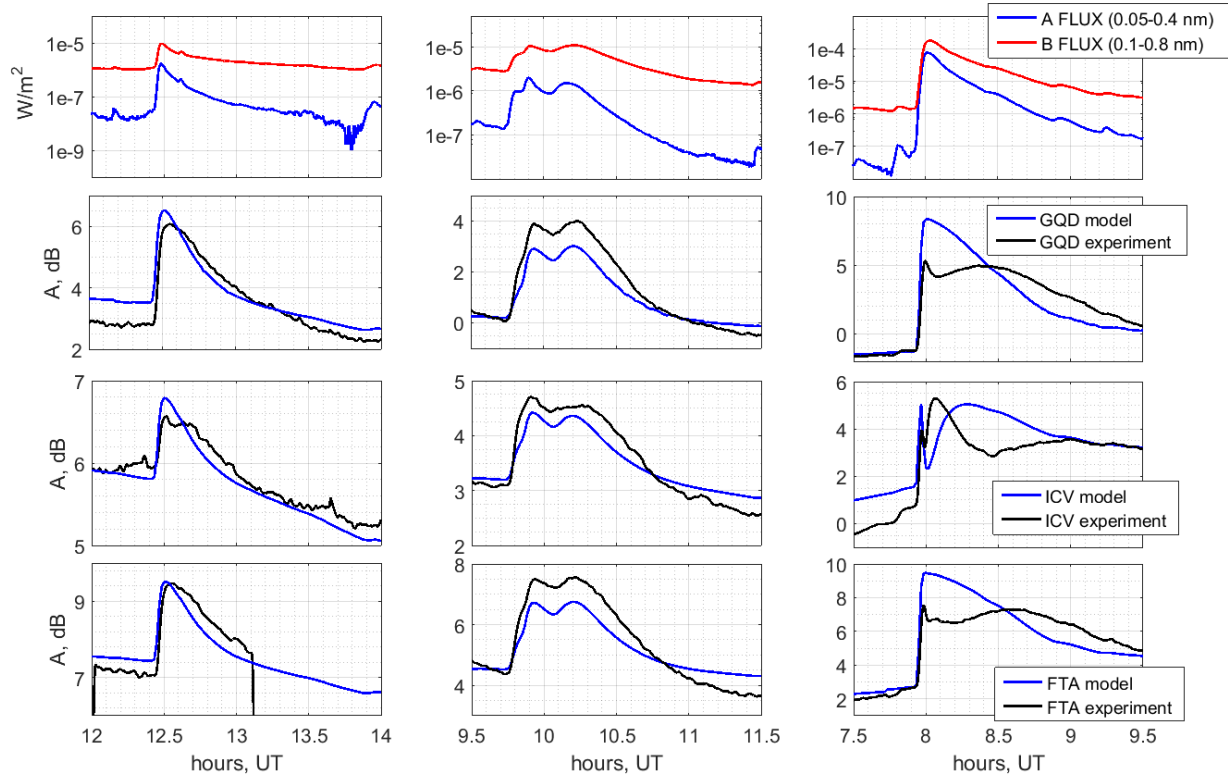
276   **Figure 6.** *X*-ray flux from the GOES satellite (top left panel) during the C-class flare on 9 June
277   2014, (top middle panel) M-class flare on 25 October 2013 and (top right panel) X-class flare on
278   25 October 2013. Theoretical and experimental time variation of amplitudes of the radio waves
279   (left panels) during the *C*-class flare on 9 June 2014, (middle panels) *M*-class flare on 25 October
280   2013 and (right panels) *X*-class flare on 25 October 2013, received from the GQD, ICV, FTA
281   transmitters.

282   It is found out that the constructed plasma-chemical model allows us to predict the
283   amplitude response to the *C*- and *M*-class flares with sufficiently high accuracy, which is evident
284   from the left and middle panels of Figure 6. Moreover, three recurrent flares of *C*-class that
285   occurred on 10 June 2014 are correctly simulated on 5 paths out of 6, which means the low
286   influence of the dynamics of small neutral components.

287   As for the *M*-class flare, verification of the built lower ionosphere model according to the
288   radiophysical data has showed that the model allows describing not only the qualitative variation
289   of the experimental value of amplitude, but also its quantitative response to the ionization

290   growth. The difference between the experimental and calculated values is maximum during the
291   highest ionization rate, being within a range of 1dB for all considered paths.

292   Despite the insignificant difference between the simulated and experimental values, it
293   was not possible to describe the qualitative variation of the signal amplitude in some cases. For
294   example, the theoretical amplitude values for the path ICV–Mikhnevo during the *M*-class flares
295   that occurred on 24 October 2013 keep growing, while the experimental *A* values demonstrate
296   the drastic decrease and vice versa.

297   The right part of Figure 6 presents the results of simulating the ionospheric response to a
298   *X*-class flare. The amplitude dynamics simulation is not correct in the part following after the
299   flare start at 08:00 UT. Analysis of the Sun's radiation spectrum, based on the RHESSI
300   observatory data has proved presence of ultrahard *X*-radiation in this flare, not described by the
301   current heuristic model of the radiation spectrum and ionization of the lower ionosphere
302   (Korsunskaja, 2019).

303   A similar result was obtained for the ICV station on 10 June 2014, i.e. the correct
304   modeling of the response to three consecutive flares of *C*-class up to 11:00 UT, and a significant
305   quantitative error at the simulation of two flares of *X*-class at 11:30–14:00 UT (Figure 7).
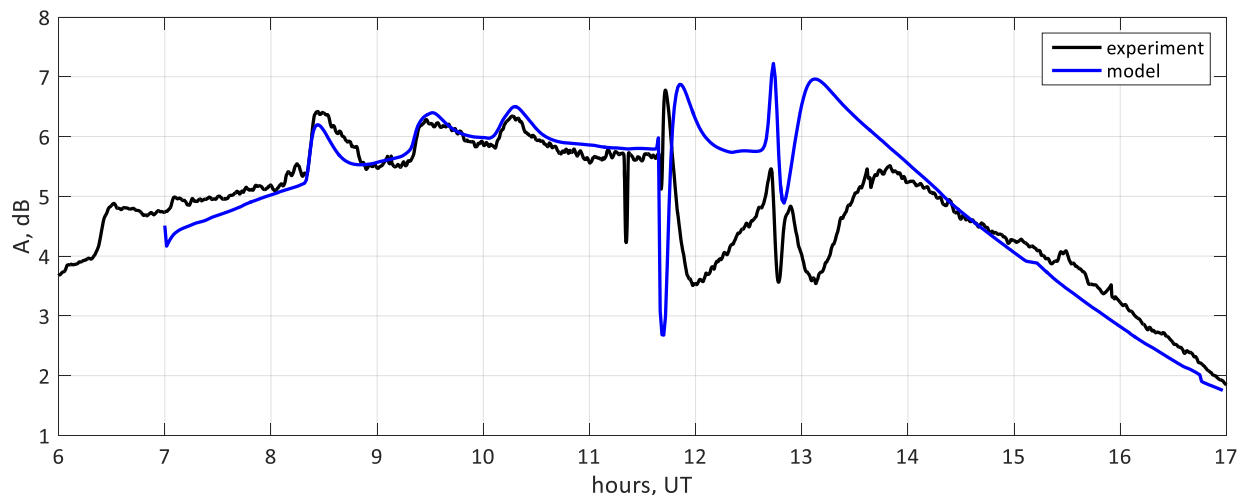

306
307   **Figure 7.** The theoretical and experimental time variation of amplitude of the radio wave due to
308   the *X*-ray flares of *C*- and *X*-class on 10 June 2014, received from the ICV transmitter.

309   The following work will include further development of the ionization model aimed at
310   the correct account of the ultrahard *X*-radiation, and its advanced verification for all available
311   paths and transmitter frequencies.

312   In addition to qualitative evaluation of the results obtained, we analyzed the quantitative
313   difference in [dB] between the simulated and experimental values of the radio wave amplitude
314   during the flares considered. For this purpose, a function $D(t) = A_{theor}(t) - A_{exp}(t)$ for 4 days
315   including the days with solar flares listed in Table 2 was analyzed.

316   As criteria of quality of the obtained results we selected two parameters - the root mean
317   square error (RMSE) and the $D(t)$ module integral rationed by the integration time interval, given
318   in formulas (2), (3):

$$\sigma = \sqrt{\frac{\sum_{i=1}^{n}(D_i(t))^2}{n}} ; \tag{2}$$

$$I = \frac{\int_{t_1}^{t_2}|D(t)|dt}{t_2 - t_1} . \tag{3}$$

319   It is obvious that the smaller the values of these parameters, the better the model
320 describes the measured values of the signal amplitude.

321   Figure 8 shows the obtained values of RMSE and *I* averaged for each class of the flares.
322 On the left, the diagrams are provided with indication of the transmitters from Table 1 and the
323 frequencies at which they operate. Red color shows the lines corresponding to the *X*-class flares,
324 yellow is for *M*-class, green – for *C*-class.
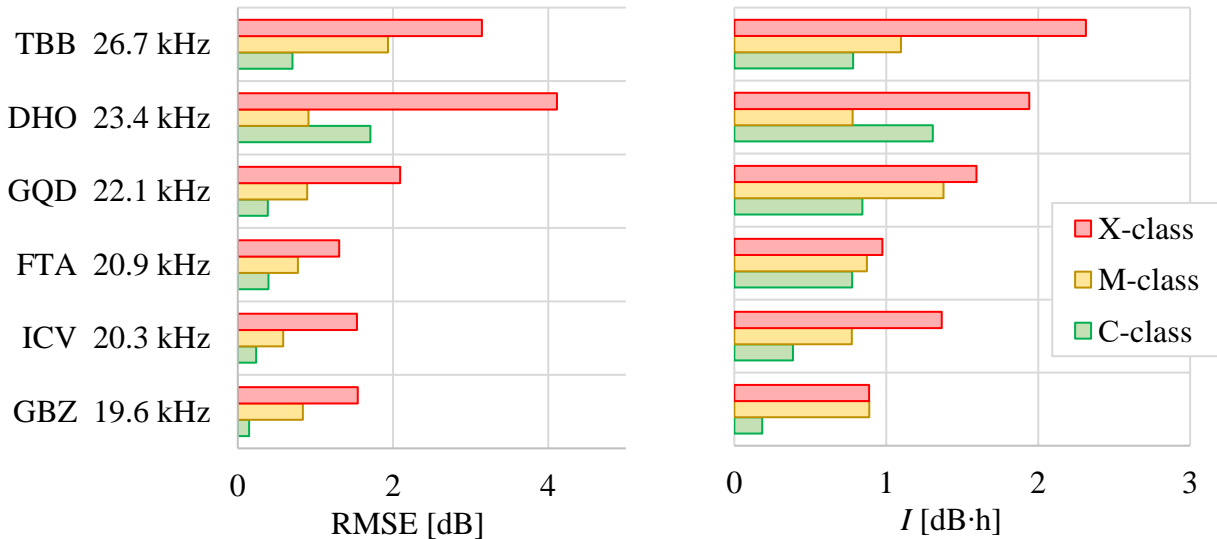
325
326 **Figure 8.** Average values of (left panel) RMSE and (right panel) *I* for six VLF paths.

327   Additionally, we calculated RMSE and *I* separately for the time intervals corresponding
328 to the ionization growth, i.e. up to the moment when the radiation flux measured on the GOES
329 satellite becomes maximum, and the periods of relaxation after maximums. It is found that the
330 calculated parameters corresponding to the different periods of a flare are almost the same, that is
331 why we do not provide them here.

332   The obtained criteria provided in Figure 8 confirms the conclusion made at the qualitative
333 evaluation of the theoretical and experimental results agreement; the smaller is the class of
334 simulated flare, the better it is described with use of the constructed model. The only exception is
335 the results obtained for the path DHO–Mikhnevo, i.e. the lowest criteria values correspond to the
336 *M*-class flares on this path.

337   In addition to the dependence on the flare energy, one can notice some correlation of the
338 results with the transmitter frequency. For example, simulated data for the paths from lower
339 frequency transmitters – GBZ, ICV, FTA, and GQD have a better agreement with the

340 experimental data for the *X*-class flares. At the same time, there is a significant difference in the
341 path lengths of the transmitters - GBZ, ICV, FTA, GQD and those from DHO and TBB. The two
342 latter show the worse agreement with the experiment. Thus, in terms of modeling high energy
343 flares, the issue of correct calculation of the electron concentration profile defining the geometry
344 of the waveguide remains undecided.

345 As a result of the verification with use of the data of ground-based radiophysical
346 measurements taken at the Mikhnevo geophysical observatory it is found that the RMSE does
347 not exceed 1 dB for ~80% of cases including *X*-class flares during which the amplitude jump on
348 some paths reaches 8 dB. Qualitative and quantitative analysis of the verification results of the
349 VLF signal amplitude has showed the good predictive capability of the built model for
350 describing weak and moderate ionospheric disturbances.

5 Conclusions

352 The results of verification of the model simulating the ionospheric *D*-region, performed
353 according to the ground-based radiophysical measurements taken at the Mikhnevo geophysical
354 observatory prove that application of the satellite data of the neutral atmosphere and the
355 ionization rates calculated on the basis of the actual radiation flux values within the *X*-ray and
356 ultraviolet ranges, allows us to describe the lower ionosphere during the *C*- and *M*-class flares
357 with sufficient accuracy. Also, it should be emphasized that a year of high solar activity is
358 characterized by the *C*-class flare level of the background *X*-ray flux. This means that the
359 additional ionization of the lower ionosphere by *X*-ray radiation must be taken into account at
360 any time rather than only at the time of the actual large flare.

361 When simulating the ionosphere under the condition of the *X*-class flares, we have
362 obtained contradicting results. In our opinion, the main reason for significant errors occurring at
363 *D*-region modeling during the high-level of ionization is the unaccounted ultrahard *X*-radiation.
364 This leads to the inaccurate calculation of the electron concentration profile and, consequently,
365 errors at determining the absolute value of the amplitude response to a sharp growth of
366 ionization. Consequently, this affects the accuracy of describing the environment relaxation after
367 the disturbance. At the same time, we note that the model recovers the background amplitude
368 varying by ~0.5 dB from the experimental value within 1–2 hours after the *X*-class flare event.

References

386 Anderson, G. P., Clough, S. A., Kneizys, F. X., Chetwynd, J. H., & Shettle, E. P. (1986).
387 Atmospheric Constituent Profiles (0-120km). *Environmental research papers*. (No. 954).
388 Hanscom, MA: Air Force Geophysics Laboratory.

389 Bekker, S. Z. (2018). Analysis of electron density calculations using deterministic-probabilistic
390 model of the ionospheric D-region. *Solar-Terrestrial Physics*, 4(3), 67–75.
391 https://doi.org/10.12737/stp-43201809

392 Bekker, S. Z., Lyakhov, A. N., Kozlov, S. I., & Ryakhovskiy, I. A. (2018). Verification of the
393 deterministic-probabilistic model of the D–region of the ionosphere by the radio physical data
394 obtained in the geophysical observatory Mikhnevo. *Proceedings of SPIE*, 108339P.
395 https://doi.org/10.1117/12.2504295

396 Bilitza, D., Altadill, D., Truhlik, V., Shubin, V., Galkin, I., Reinisch, B., & Huang, X. (2017).
397 International Reference Ionosphere 2016: from ionospheric climate to real-time weather
398 predictions. *Space Weather*, 15(2), 418–429. https://doi.org/10.1002/2016SW001593

399 Brunelli, B. E., & Namgaladze, A. A. (1988). *Physics of the ionosphere*. Moscow: Nauka.

400 Egorova, T., Rozanov, E., Ozolin, Y., Shapiro, A., Calisto, M., Peter, T., & Schmutz, W. (2011).
401 The atmospheric effects of October 2003 solar proton event simulated with the chemistry-climate
402 model SOCOL using complete and parameterized ion chemistry. *Journal of Atmospheric and
403 Solar-Terrestrial Physics*, 73, 356–365. https://doi.org/10.1016/j.jastp.2010.01.009

404 Egoshin, A. A., Ermak, V. M., Zetzer, Yu. I., Kozlov, S. I., Kudryavtsev, V. P., Lyakhov, A. N.,
405 et al. (2012). Influence of meteorological and wave processes on the lower ionosphere during solar
406 minimum conditions according to the data on midlatitude VLF–LF propagation. *Physics of the
407 Solid Earth*, 48(3), 275–286. https://doi.org/10.1134/S1069351312030020

408 Ferguson, J. A. (1995). Ionospheric model validation at VLF and LF. *Radio Science*, 30(3), 775–
409 782. https://doi.org/10.1029/94RS03190

410 Ferguson, J. A. (1998). Computer Programs for Assessment of Long-Wavelength Radio
411 Communications, Version 2.0., Technical document 3030. San Diego, CA: Space and Naval
412 Warfare Systems Center.

413 Friedrich, M., Pock, C., & Torkar, K. (2018). FIRI-2018, an updated empirical model of the lower
414 ionosphere. *Journal of Geophysical Research: Space Physics*, 123, 6737–6751.
415 https://doi.org/10.1029/2018JA025437

416 Gavrilov, B. G., Ermak, V. M., Poklad, Yu. V., & Ryakhovskii, I. A. (2019a). Estimate of
417 Variations in the Parameters of the Midlatitude Lower Ionosphere Caused by the Solar Flare of
418 September 10, 2017. *Geomagnetism and aeronomy*, 59(5), 587–592.
419 https://doi.org/10.1134/S0016793219050049

420 Gavrilov, B. G., Zetser, Yu. I., Lyakhov, A. N., Poklad, Yu. V., & Ryakhovskii, I. A. (2017).
421 Spatiotemporal Distributions of the Electron Density in the Ionosphere by Records of the Total
422 Electron Content and Phase of VLF Radio Signals. *Geomagnetism and aeronomy*, 57(4), 461–470.
423 https://doi.org/10.1134/S0016793217040065

424 Gavrilov, B. G., Zetser, Yu. I., Lyakhov, A. N., Poklad, Yu. V., & Ryakhovskii, I. A. (2019b).
425 Correlated Disturbances of the Upper and Lower Ionosphere from Synchronous Measurements of
426 Parameters of GNSS Signals and VLF Radio Signals. *Cosmic Research*, 57, 36–43.
427 https://doi.org/10.1134/S0010952519010039

428 Glukhov, V. S., Pasko, V. P., & Inan U. S. (1992). Relaxation of transient lower ionospheric
429 disturbances caused by lightning-whistler-induced electron precipitation bursts. *Journal of
430 Geophysical Research*, 97(A11), 16971–16979. https://doi.org/10.1029/92JA01596

431 Machol, J., & Viereck, R. (2016). GOES X-ray Sensor (XRS) Measurements. Version 1.4.1. URL:
432 https://www.ngdc.noaa.gov/stp/satellite/goes/doc/GOES_XRS_readme.pdf.   NOAA   National
433 Centers for Environmental Information (NCEI), University of Colorado, Cooperative Institute for
434 Research in Environmental Science (CIRES), NOAA Space Weather Prediction Center (SWPC).

435 Grubor, D., Sulic, D., & Zigman, V. (2005). Influence of solar X-ray flares on the earth-ionosphere
436 waveguide. *Serbian Astronomical Journal*, 171, 29–35. https://doi.org/10.2298/SAJ0571029G

437 Grubor, D., Sulic, D., & Zigman, V. (2008). Classification of X-ray solar flares regarding their
438 effects on the lower ionosphere electron density profile. *Ann. Geophysics*, 26(7), 1731–1740.
439 https://doi.org/10.5194/angeo-26-1731-2008

440 Han, F., Cummer, S. A., Li, J., & Lu, G. (2011). Daytime ionospheric D region sharpness derived
441 from VLF radio atmospherics. *Journal of Geophysical Research*, 116, A05314.
442 https://doi.org/10.1029/2010JA016299

443 Hargreaves, J. K. (1995). The solar-terrestrial environment. Cambridge, UK: Cambridge
444 University Press.

445 Hedin, A. E. (1991). Extension of the MSIS Thermospheric Model into the Middle and Lower
446 Atmosphere. *Journal of Geophysical Research*, 96(A2), 1159–1172.
447 https://doi.org/10.1029/90JA02125.

448 Korsunskaja, J. A. (2019). Heuristic model of solar x-ray spectrum according to satellite data for
449 geophysical applications. *Solar-Terrestrial Physics*, 5(3), 75–86. https://doi.org/10.12737/stp-
450 53201909

451 Krivolutsky, A. A., Cherepanova, L. A., V'yushkova, T. Y., & Repnev, A. I. (2015). The three-
452 dimensional global numerical model CHARM-I: The incorporation of processes in the ionospheric
453 D-region.   *Geomagnetism   and   aeronomy,*   55(4),   467–486.
454 https://doi.org/10.1134/S0016793215030123

455 Kudryavtsev, V.P., Romanyukha, N.Yu. (1995). Modelling of ionization-recombination processes
456 in the middle atmosphere. *Mathematical Modeling*, 7(3), 3–18.

457 Kumar, A., & Kumar, S. Earth Planets Space (2018). 70: 29. https://doi.org/10.1186/s40623-018-
458 0794-8

459 Kumar, S., Kumar, A., Menk, F., Maurya, A. K., Singh, R., & Veenadhari, B. (2015). Response
460 of the low-latitude D region ionosphere to extreme space weather event of 14–16 December 2006.
461 *Journal   of   Geophysical   Research: Space   Physics*,   120,   788–799.
462 https://doi.org/10.1002/2014JA020751

463 Kumar, S., NaitAmor, S., Chanrion, O., & Neubert, T. (2017). Perturbations to the lower
464 ionosphere by tropical cyclone Evan in the South Pacific region. *Journal of Geophysical Research:*
465 *Space Physics*, 122, 8720–8732. https://doi.org/10.1002/2017JA024023

466 Livesey, N.J., Read, W.G., Lambert, A., Cofield, R.E., Cuddy D.T., Froidevaux L., et al. (2013).
467 Aura Microwave Limb Sounder (MLS). Version 2.2 and 2. URL: https://mls.jpl.nasa.gov/data/v2-
468 2_data_quality_document.pdf. California Institute of Technology, Pasadena, California.

469 Lyakhov, A. N., Korsunskaya, J. A., Gavrilov, B. G., Ryakhovskiy, I. A., Bisyarin, M. A., Kirillov,
470 V. V., et al. (2018). Verification of the empirical lower ionosphere models on VLF observations
471 at midlatitude Mikhnevo geophysical observatory. *Proceedings of SPIE*, 108339N.
472 https://doi.org/10.1117/12.2504293

473 Marsh, D. R., Mills, M., Kinnison, D., Lamarque, J.-F., Calvo, N., & Polvani, L. (2013). Climate
474 change from 1850 to 2005 simulated in CESM1 (WACCM). *Journal of Climate*, 26(19), 7372–
475 7391. https://doi.org/10.1175/JCLI-D-12-00558

476 Maurya, A. K., Veenadhari, B., Singh, R., Kumar, S., Cohen, M. B., Selvakumaran, R., et al.
477 (2012). Nighttime D region electron density measurements from ELF-VLF tweek radio
478 atmospherics recorded at low latitudes. *Journal of Geophysical Research*, 117, A11308.
479 https://doi.org/10.1029/2012JA017876

480 Maurya, A. K., Venkatesham, K., Kumar, S., Singh, R., Tiwari, P., & Singh, A. K. (2018). Effects
481 of St. Patrick's Day geomagnetic storm of March 2015 and of June 2015 on low-equatorial D
482 region ionosphere. *Journal of Geophysical Research: Space Physics*, 123, 6836–6850.
483 https://doi.org/10.1029/2018JA025536

484 Mitra, A.P. (1974). *Ionospheric Effects of Solar Flares*. Dordrecht: Reidel.

485 Nava, B., Coïsson, P., & Radicella, S. M. (2008). A new version of the NeQuick ionosphere
486 electron density model. *Journal of Atmospheric and Solar-Terrestrial Physics*, 70(15), 1856–1862.
487 https://doi.org/10.1016/j.jastp.2008.01.015

488 Nina, A., Cadez, V., Sulic, D., Sreckovic, V., & Zigman, V. (2011). Effective electron
489 recombination coefficient in ionospheric D-region during the relaxation regime after solar flare
490 from February 18, 2011. *Nuclear Instruments and Methods in Physics Research B*, 279, 106–109.
491 https://doi.org/10.1016/j.nimb.2011.10.026

492 Palit, S., Basak, T., Mondal, S. K., Pal, S., & Chakrabarti, S. K. (2013). Modelling of the Very
493 Low Frequency (VLF) radio wave signal profile due to solar flares using the GEANT4 Monte
494 Carlo simulation coupled with ionospheric chemistry. *Atmospheric Chemistry and Physics*, 13,
495 9159–9168. https://doi.org/10.5194/acp-13-9159-2013

496 Paulsen, D. E., Huffman, R. E., & Larrabe, J. C. (1972). Improved photoionization rates of $O_2(^1\Delta_g)$
497 in the D – region. *Radio Science*, 7(1), 51–55. https://doi.org/10.1029/RS007i001p00051

498 Peter, W. B., Chevalier, M. W., & Inan, U. S. (2006). Perturbations of mid-latitude subionospheric
499 VLF signals associated with lower ionospheric disturbances during major geomagnetic storms.
500 *Journal of Geophysical Research*, 111, A03301. https://doi.org/10.1029/2005JA011346

501 Poppoff, I. G., & Whitten, R. C. (1962). D-Region Ionization by Solar X Rays. *Journal of*
502 *Geophysical Research*, 67(7), 2986–2988. https://doi.org/10.1029/JZ067i007p02986

503 Ryakhovskiy, I. A., Gavrilov, B. G., Lyakhov, A. N., Poklad, Y. V., Bekker, S. Z., & Kozlov, S.
504 I. (2018). Ionization of the lower ionosphere during the X-ray solar flare on September 6, 2017.
505 *Proceedings of SPIE*, 108339Y. https://doi.org/10.1117/12.2504402

506 Schunk, R. W., & Nagy A. (2009). Ionospheres: Physics, Plasma Physics, and Chemistry.
507 Cambridge, UK: Cambridge University Press.

508 Thomas, L., & Bowman, M. R. (1985). Model studies of the D-region negative-ion composition
509 during day-time and night-time. *Journal of Atmospheric and Solar-Terrestrial Physics*, 47(6),
510 547–556.

511 Thomson, N. R., Rodger, C. J., & Clilverd, M. A. (2005). Large solar flares and their ionospheric
512 D region enhancements. *Journal of Geophysical Research*, 110(A9), 6306.
513 https://doi.org/10.1029/2005JA011008

514 Thomson, N. R., Rodger, C. J., & Dowden, R. L. (2004). Ionosphere gives size of greatest solar
515 flare. *Geophysical Research Letters*, 31, L06803. https://doi.org/10.1029/2003GL019345

516 Turunen, E., Matveinen H., & Ranta H. (1992). Sodankyla Ion Chemistry (SIC) model. Rept. 49.
517 Finland: Sodankyla Geophysical Observatory.

518 Turunen, E., Tolvanen, J., Matveinen, H., & Ranta H. (1996). D Region Ion Chemistry Model.
519 *STEP Handbook of Ionospheric Models* (pp. 1–25). Boulder, CO: Utah State University.

520 Verronen, P. T., Andersson, M. E., Marsh, D. R., Kovacs, T., & Plane, J. M. C. (2016). WACCM-
521 D – Whole atmosphere community climate model with D-region ion chemistry. *Journal of*
522 *Advances in Modeling Earth Systems*, 8(2), 954–975. https://doi.org/10.1002/2015MS000592

523 Verronen, P. T., Seppala, A., Clilverd, M. A., Rodger, C. J., Kyrola, E., Enell, C.-F., et al. (2005).
524 Diurnal variation of ozone depletion during the October-November 2003 solar proton events.
525 *Journal of Geophysical Research*, 110, A09S32. https://doi.org/10.1029/2004JA010932

526 Wait, J. R., & Spies, K. P. (1964). Characteristics of the Earth-ionosphere waveguide for VLF
527 radio waves. NBS Technical Note 300. Washington, US.

528 Woods, T.N., Eparvier, F.G., Hock, R., Jones, A.R., Woodraska, D., Judge, D., et al. (2012).
529 Extreme Ultraviolet Variability Experiment (EVE) on the Solar Dynamics Observatory (SDO):
530 Overview of science objectives, instrument design, data products, and model developments. *Solar*
531 *Phys*ics, 275, 115–143. https://doi.org/10.1007/s11207-009-9487-6.